*energies*

MDPI

*Article*

# Numerical Simulation of Gas-Solid Two-Phase Heat Transfer in a Kaolin Cyclone Cooling System

**Shuai Xu [1], Junlin Xie [1], Shuxia Mei [1,*], Feng He [1], Runguo Li [2], Yuhua Deng [2], Chao Zhang [2] and Xianming Zheng [2]**

[1] School of Materials Science and Engineering, Wuhan University of Technology, Wuhan 430070, China
[2] CBMI Construction Co., Ltd., Beijing 100176, China
* Correspondence: msx0303@163.com

**Abstract:** The kaolin suspension calcination technology is currently gaining attention as a new process of calcining kaolin. In this paper, the cooling system of the kaolin suspension calcination process designed by CBMI Construction Co., Ltd. is simulated using ANSYS Fluent software to analyze the velocity field and temperature field of the gas–solid two-phase flow using the Eulerian model. A compiled UDF (User-Defined Function) is used to simulate the transfer of mass and heat from the downcomer tube to the different elements. The gas, coming from the gas outlet of the cyclone, enters the next level twin-cylinder cyclone in a spiral state. The results show that the airflow in the cyclone consists of an external spiral flow from the top to the bottom and an internal spiral flow from the bottom to the top. During the downward movement of the airflow, the outer spiral flow is continuously transformed into an inner cyclonic flow. The part of the airflow that rotates close to the inner cylinder is likely to become a 'short circuit flow', which largely affects the separation efficiency and cooling effect of the cyclone. There is evident temperature deviation and flow deviation in the twin-cylinder cyclone, which is primarily due to the high cooling air volume and high rotation of air flow coming from the gas outlet of the previous level's cyclone. The rotation of the air flow is the main cause of the bias temperature and bias flow phenomenon in the twin-cylinder cyclone.

**Keywords:** cyclone; numerical simulation; heat transfer; Eulerian model; kaolin suspension calcination technology; cooling systems



**Citation:** Xu, S.; Xie, J.; Mei, S.; He, F.; Li, R.; Deng, Y.; Zhang, C.; Zheng, X. Numerical Simulation of Gas-Solid Two-Phase Heat Transfer in a Kaolin Cyclone Cooling System. *Energies* **2023**, *16*, 3744. https://doi.org/10.3390/en16093744

Academic Editor: Antonio C.M. Sousa

Received: 6 March 2023
Revised: 23 April 2023
Accepted: 25 April 2023
Published: 27 April 2023



## 1. Introduction

$CO_2$ emissions from the cement industry account for approximately 7% of the global anthropogenic $CO_2$ emissions [1]. The International Energy Agency published possible measures to reduce $CO_2$ emissions in its Cement Technology Roadmap in 2009. One of the most widely discussed measures is the use of supplementary cementitious materials (SCMs) as a replacement for clinker to reduce $CO_2$ emissions during clinker production [2]. However, with countries such as the USA, the UK, and the Netherlands announcing the closure of power plants around 2030, the supply chain of slag and fly ash, which are traditional SCM materials, has been significantly reduced [3]. As a result, researchers are looking for related clay minerals such as kaolin as a more practical SCM material for the future due to their wide distribution and large storage capacity. However, the traditional rotary kiln calcination process tends to agglomerate the clay and reduce the activity of the product, making the development of new calcination processes a focus of research in the field of calcined kaolin [4].

The suspension calcining technology has garnered considerable attention from the cement industry as a novel process. Similar to the new dry process in cement production, this method is divided into three key stages: Preheating, calcination, and cooling systems [5]. In contrast to the cooling system with a cooler for the cement production process [6], the kaolin suspension calcination process is based on a cyclone as a cooling system [7]. Cyclone

separators are equipment that use centrifugal force to separate particles from the airflow and conduct heat exchange between gas and solid. They are widely used in almost all industries requiring gas-solid separation, from chemical to biopharmaceuticals [8,9].

At present, there are many studies on cyclone separators in new dry-process cement production technology, but the complexity of the internal flow field makes it difficult for theoretical and experimental studies to be carried out. The rapid development of computer technology increasingly encourages researchers to use computational fluid dynamics (CFD) to solve the problem of cyclone separators. Studies on the use of CFD to study cyclone separators are numerous, enough to prove its superiority compared to traditional experimental methods [10–14].

However, in most CFD studies of the internal flow field of cyclone cylinders, the flow field distribution characteristics in the heat exchanger are not taken into account, and modeling starts directly from the volute part, or the vertical velocity inlet boundary condition in the heat exchange pipe of cyclone preheater is used to replace the spiral velocity inlet boundary condition, which leads to differences between the modeling result and the actual conditions in the cyclone cylinder [15–19]. In fact, the air spirals upward and enters the heat exchanger pipe of the next level of the cyclone cylinder when it leaks out of the outlet of the previous level of the cyclone cylinder. The difference in boundary conditions will inevitably lead to deviation of the flow. For the lowermost level of the cyclone cylinder, the difference caused by ignoring the gas flow field in the heat exchanger is not very obvious, but for the level that contains a double cyclone cylinder, such simplification will result in significant differences.

Therefore, to make the model more realistic, this study models the whole cooling system consisting of two cyclone separators. On the other hand, many researchers only focus on the separation efficiency of cyclones, and there are few studies on the heat transfer performance of cyclones, let alone a systematic analysis of temperature changes inside cyclones [20,21]. In view of this, the coupling process between a gas and a solid is considered in this model. The presence of the cyclone's downcomer tube may allow a portion of the airflow to enter it, affecting the normal flow of air. The transfer of the mass of raw meals between the different cyclones is simulated by a compiled UDF (User-Defined Function). The above treatment will ensure the research results are more in line with the actual engineering situation.

In this paper, the cyclone cooling system of the kaolin suspension calcination process designed by CBMI Construction Co., Ltd. was simulated using ANSYS FLUENT 15.0 software, aiming to investigate the movement of airflow within the cyclone, and predicting the cooling effect of this cooling system on metakaolin. The research results will provide an important theoretical reference for the rational design of cyclone cooling systems in the kaolin suspension calcination process.

## 2. Geometric Models and Meshes

The geometrical model and mesh division of the CC1-CC2 cyclone cooling system is shown in Figures 1 and 2, respectively. The height of the entire system is 10.25 m, and the dimensions of the outer and inner cylinders of the cyclone are shown in Table 1. As shown in Figure 1, the cooling system is composed of two cyclones, CC1 and CC2. The cold air enters the system from the bottom CC1 inlet from bottom to top, flows through CC1 and CC2, respectively, and finally escapes from the flue gas outlet at the top of CC2. The hot metakaolin enters the CC2 heat exchanger tube, eventually exiting through the bottommost metakaolin outlet. The schematic diagram of the air flow in the cooling system is shown in Figure 1b.

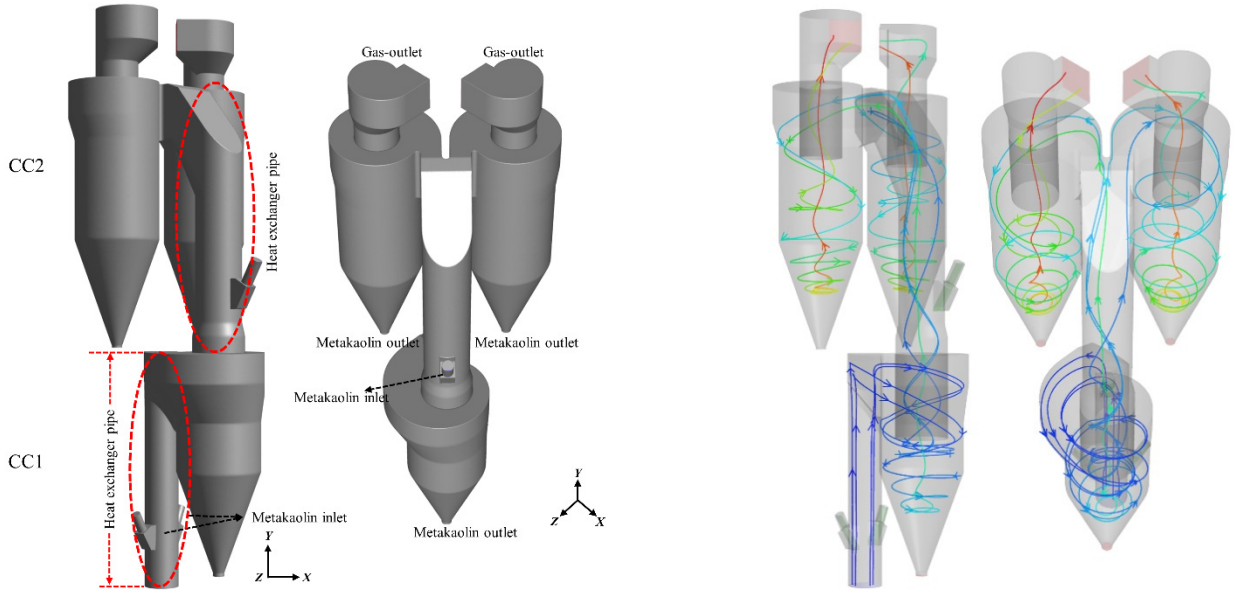


(**a**) Cooling system model (**b**) The diagram of the air flow

**Figure 1.** Cooling system model and diagram of the air flow.

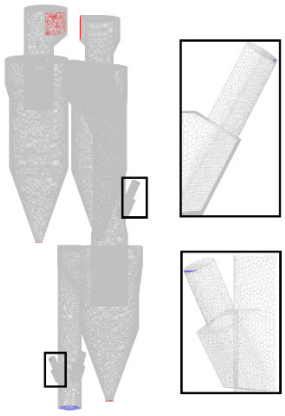

**Figure 2.** Mesh.

**Table 1.** The dimensions of CC1 and CC2.

| Type | CC1 Cylone | | CC2 Cylone | |
|---|---|---|---|---|
| | Inner Cylinder | Outer Cylinder | Inner Cylinder | Outer Cylinder |
| Diameter (m) | 1.6 | 2.56 | 1.3 | 2.56 |

The grid division of the cooling system is shown in Figure 2, which uses a polyhedral mesh. Compared to structured meshes, unstructured meshes have a more random distribution of mesh nodes, making them more suitable for dealing with bends and irregular boundaries. Due to the presence of structures such as heat exchange pipes, volute, and the discharge box in the model, with sharp corners and geometric transitions on the connecting parts, an unstructured mesh is more suitable for covering irregular regions and handling these areas compared to structured meshes. The polyhedral mesh is a recent development in unstructured meshing and is an optimization of tetrahedral and pentahedral meshes. Polyhedral meshes have higher mesh quality, faster convergence, and are easier to generate [22,23]. Taking into account the high density of metakaolin particles near the dispensing box and the potential for high local turbulence viscosity just after the particles come into contact with the airflow, the mesh was locally refined near the bottom wall of the dispensing box to achieve higher computational accuracy [24].

In the simulation process, in order to ensure the accuracy of the calculation, it is necessary to determine whether the simulation results change with the number of grids, that is, to verify the grid independence. Figure 3 shows the curve of the average temperature of particles at the metakaolin outlet of CC1 as a function of the total amount of cooling system grids. It can be found that when the number of cells is greater than 1.22 million, the average outlet temperature is basically unchanged, and the fluctuation is within the allowable error range. At this point, the results of the calculation are already largely independent of the number of grids, so this number of grids is used for calculation.

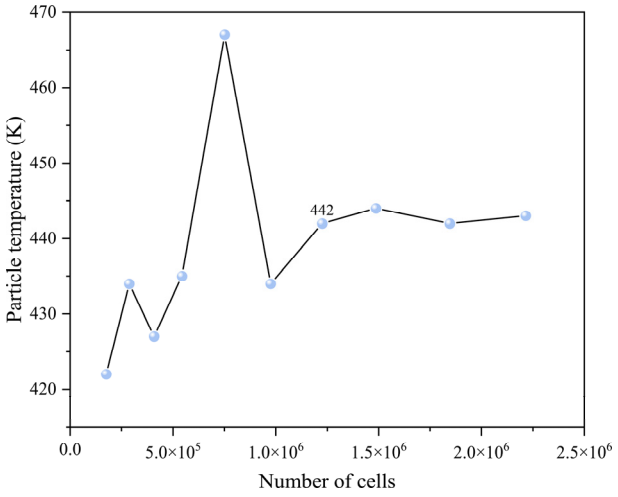


**Figure 3.** Mesh dependence test.

## 3. Numerical Model and Boundary Conditions

### *3.1. Numerical Model*

For the gas-phase turbulence model, the Reynolds Stress Model (RSM) is selected. This model considers the effects of rotating flow and changing surface curvature of the flow direction and is suitable for cyclones with more swirling. Compared to Large Eddy Simulation (LES), the RSM model usually has sufficient accuracy with less computer memory and less time ([25], pp. 1819–1821). Based on the RSM model, due to particle collisions and turbulence near the walls of the cyclone separator, the enhanced wall treatment model was selected to obtain better accuracy. The model is defined as:

$$\frac{\partial(\overline{u_i'u_j'})}{\partial t} + \frac{\partial(\rho u_k \overline{u_i'u_j'})}{\partial x_k} = D_{Tij} + D_{Lij} + P_{ij} + \phi_{ij} + \varepsilon_{ij} \quad (1)$$

$$\phi_{ij} = \phi_{ij,1} + \phi_{ij,2} + \phi_{ij,w} \quad (2)$$

$$\phi_{ij,1} = -C_1\rho\frac{\varepsilon}{k}\left(\overline{u_i'u_j'} - \frac{2}{3}k\delta_{ij}\right) \quad (3)$$

$$\phi_{ij,2} = -C_2\left(P_{ij} - \frac{2}{3}P\delta_{ij}\right) \quad (4)$$

$$\begin{aligned}\phi_{ij,w} = \; & C_1'\rho\frac{\varepsilon}{k}\left(\overline{u_k'u_m'}n_k n_m\delta_{ij} - \frac{3}{2}\overline{u_i'u_j'}n_j n_k - \frac{3}{2}\overline{u_j'u_k'}n_i n_k\right)\frac{k^{3/2}}{C_l\varepsilon d} \\ & + C_2'\left(\phi_{km,2}n_k n_m\delta_{ij} - \frac{3}{2}\phi_{ik,2}n_j n_k - \frac{3}{2}\phi_{ik,2}n_i n_k\right)\frac{k^{3/2}}{C_l\varepsilon d}\end{aligned} \quad (5)$$

where $D_{Tij}$ represents the turbulent diffusion equation, $D_{Lij}$ represents the molecular diffusion equation, $P_{ij}$ is the stress production equation, $\varepsilon_{ij}$ indicates the dissipation, and $\phi_{ij}$ is the pressure strain equation. $\Phi_{ij}$ is formed by summing the following three equations, where the $C_1$, $C_2$, $C_1'$, and $C_2'$ are default values.

The Eulerian model is used to calculate the gas–solid coupling process in the cyclone. During the iteration, it can simultaneously solve the mass, momentum, and energy equations of the gas-phase flow field and particles and considers the mutual effects of the two

phases ([25], pp. 2562–2565). In this paper, the Eulerian model is used for calculation. The model is defined as:

$$\frac{\partial}{\partial t}(\alpha_q \rho_q) + \nabla \cdot (\alpha_q \rho_q \vec{v}_q) = \sum_{p=1}^{n} (\dot{m}_{pq} - \dot{m}_{qp}) \tag{6}$$

$$\frac{\partial}{\partial t}(\alpha_q \rho_q \vec{v}_q) + \nabla \cdot (\alpha_q \rho_q \vec{v}_q \vec{v}_q) = -\alpha_q \nabla P + \nabla \bar{\bar{\tau}}_q + \alpha_q \rho_q \vec{g} + \vec{R}_{qp} + \vec{F} \tag{7}$$

$$\bar{\bar{\tau}}_q = \alpha_q \mu_q (\nabla \vec{v}_q + \nabla \vec{v}_q^T) + \alpha_q (\lambda_q - \tfrac{2}{3}\mu_q) \nabla \cdot \vec{v}_q \bar{\bar{I}} \tag{8}$$

$$\frac{\partial}{\partial t}(\alpha_q \rho_q h_q) + \nabla \cdot (\alpha_q \rho_q \vec{u}_q \vec{h}_q) = \alpha_q \frac{\partial p_q}{\partial t} + \bar{\bar{\tau}}_q \cdot \nabla \vec{v}_q - \nabla \cdot \vec{q}_q + Q_{pq} \tag{9}$$

where $v_q$ is the velocity of phase $q$ and $m_{pq}$ characterizes the mass transfer from the $p$th to $q$th phase, and $m_{qp}$ characterizes the mass transfer from phase $q$ to phase $p$. $\tau_q$ denotes the stress–strain tensor, μ and λ denote the shear viscosity and bulk viscosity, respectively, and $F$ is the force to which the particles are subjected, such as drag, lift, and turbulence dispersion, etc. Drag has been considered among these forces, while others, such as lift and turbulence dispersion, have not been taken into account in this simulation. This is because these interaction forces are relatively small for the gas-solid two-phase. P is the pressure. h is the specific heat of the phase, $q$ is the thermal conductivity, and Q is the heat transfer intensity between phases.

### *3.2. Numerical Scheme*

The steady approach was utilized for this calculation. A pressure-based solver was selected. The pressure–velocity coupling algorithm uses the Phase Coupled SIMPLE. The PRESTO! scheme was adopted for pressure discretization, and the second-order upwind scheme was adopted for energy discretization, while other equations all use a first-order upwind scheme. The relaxation factors maintain the default values of the Eulerian model. The mass and temperature of the particles at each boundary are monitored, and the calculation is considered to have converged when the mass is conserved at each outlet and the temperature is almost unchanged.

### *3.3. Boundary Conditions*

The data provided by CBMI Construction were used as the boundary conditions for this simulation, as shown in Table 2.

**Table 2.** Boundary conditions.

| Boundary Type | | Temperature(K) | Gas Velocity (m/s) | Particle Volume Fraction | Particle Velocity (m/s) |
|---|---|---|---|---|---|
| | Gas-inlet | 298 | 17.9 | / | / |
| CC1 | Metakaolin-inlet1 | UDF | / | 0.1335 | 7.67 |
| | Metakaolin-inlet2 | UDF | / | 0.1335 | 7.67 |
| CC2 | Metakaolin-inlet | 910 | / | 0.1995 | 7.54 |

The pressure outlet boundary is used for all exit boundaries. The gas phase is set to air and the particle phase is the completely burned product of kaolin, i.e., metakaolin, with a mass of 9.72 kg/s fed into the CC2 cyclone separator. The relevant physical and chemical parameters are obtained from experiments. The density was measured to be 1.871 g/cm$^3$, and the particle size distribution was measured by a laser particle size analyzer and simplified to some extent. Five particle sizes were selected for setting, as shown in Table 3.

**Table 3.** Particle size.

| Diameter (μm) | 9 | 18.73 | 34.56 | 48.46 | 75.786 |
|---|---|---|---|---|---|
| Mass fraction (%) | 9.32 | 19.6 | 38.33 | 22.83 | 9.92 |

The principle of UDF in Table 2 is that before each iteration starts, the particle phase temperature of the CC2 metakaolin outlet in the previous iteration result is read and assigned to the CC1 particle inlet and used as the new boundary condition of the CC1 particle inlet for this iteration. This process continues until the temperature of the CC1 particle inlet does not change, indicating that the system is in balance and the iteration ends. This schematic diagram of the UDF is shown in Figure 4.

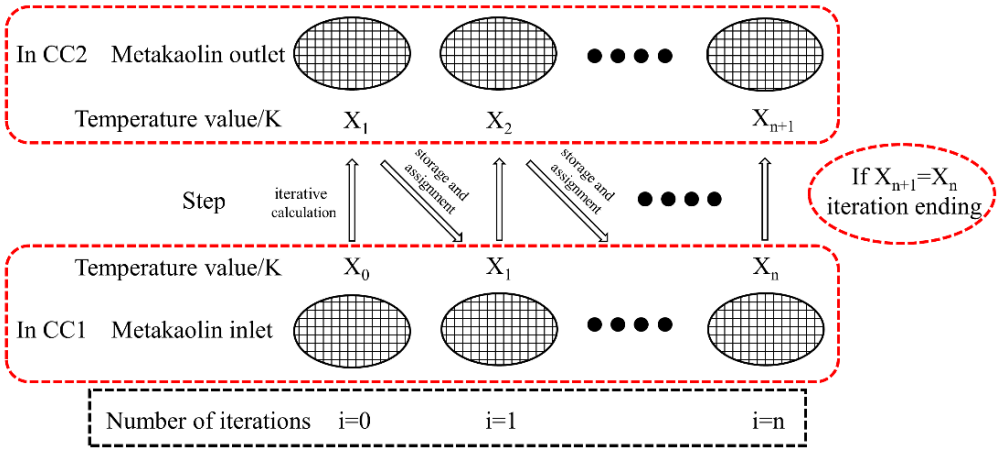


**Figure 4.** This schematic diagram of the UDF.

## 4. Model and Data Validation

As the production plant is currently in the design phase, it is crucial to determine the cooling effect of the cooling system before it is put into operation. However, since there is no actual data from the experiment to validate the reasonableness of the simulation results, it is necessary to verify the model and the simulated data using another method.

To address this issue, a cyclone preheating system for an actual cement production line was simulated under the same model, and the simulated flue gas exit temperatures were compared with the actual measured flue gas exit temperatures for the line. The working parameters of the actual production line are presented in Table 4. The results of the comparison are shown in Table 5.

**Table 4.** The actual conditions of C1–C5.

| Type | Gas Inlet Velocity (m/s) | Flue Gas Temperature (K) | Outlet Pressure (Pa) |
|---|---|---|---|
| C1 | 17.23 | 596 | −4950 |
| C2 | 18.76 | 783 | −4300 |
| C3 | 18.06 | 949 | −3170 |
| C4 | 16.94 | 1078 | −2445 |

**Table 5.** Comparison between simulated value and measured value.

| | Actual Temperature (K) | Simulated Temperature (K) | Deviation (K) | % |
|---|---|---|---|---|
| C1 | 596 | 610.2 | 14.2 | 2.4 |
| C2 | 783 | 801.4 | 18.4 | 2.3 |
| C3 | 949 | 961.3 | 12.3 | 1.3 |
| C4 | 1078 | 1085.6 | 7.6 | 0.7 |

This comparison was conducted to validate the accuracy of the simulation model and the reliability of the simulated data. With the above comparison, the accuracy of the model and the predicted data can be determined. The higher temperatures gained in the simulations could be attributed to potential air leakage or greater heat dissipation in the actual production process.

## 5. Result and Discussion

### *5.1. Gas Flow Fields*

The gas streakline is shown in Figure 5. As can be seen from Figure 5, cold air enters the system from the inlet at the bottom of CC1 and flows vertically upward. It enters the cyclone cylinder through the volute and is constrained by the cylinder wall, rotating downward along the wall to form an outer spiral flow. When the airflow reaches the bottom, it spirals upward to form an inner spiral flow and finally escapes from the outlet at the top of CC1, rotating into the heat exchanger pipe of CC2. The airflow continues to spiral upward in the heat exchanger pipe of CC2, dividing into two parts and entering the dual cyclone cylinder of CC2 to form a new dual spiral flow. Finally, the airflow after the heat exchange escapes from the air outlet at the top of CC2. According to the calculation, the maximum residence time of the airflow in the cooling system is approximately 9.13 s, of which the residence time in the heat exchanger pipe is relatively short, at only approximately 1 s.

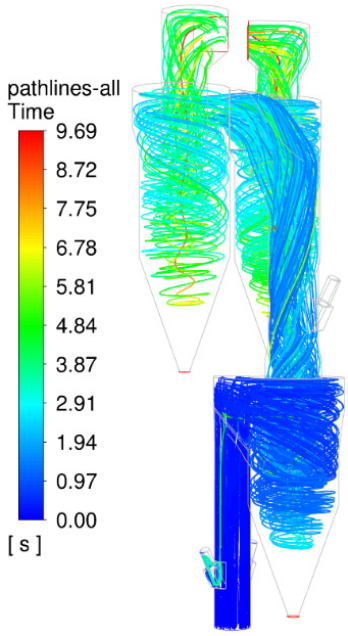


**Figure 5.** Gas streaklines.

First, the flow field inside the CC1 cyclone separator is analyzed. Unless otherwise stated, the contour plots included in this article display the contour plots of the gas phase. Figure 6 shows the velocity contours of the center axial profile of the CC1 cyclone separator. As seen in Figure 6, the gas flow velocity is maximum at the entrance of the inner cylinder, reaching 25 m/s. The gas flow velocity in the cylindrical part is relatively consistent, at approximately 15 m/s. From the cylindrical part to the conical part, the velocity value gradually decreases, and an obvious 'w'-shaped stratification appears. In the conical part, the velocity is high near the wall and low near the center.

To analyze the cause of this velocity distribution, velocity vectors of the CC1 cyclone center axial profile are further extracted, as shown in Figure 7, wherein Figure 7a represents the overall velocity distribution and Figure 7b represents the partial enlargements. From the synthesis of Figure 7a,b, it can be seen that during the process of airflow spiraling downwards from the volute part, a portion of airflow layers close to the center will directly cause a 'short circuit' in the flow to the inner cylinder inlet without rotating to the bottom. This phenomenon is caused by the influence of the pressure drop force from the wall to the center. It is worth noting that the metakaolin carried by this part of the gas will also directly enter the outlet of the cyclone, which will have a significant impact on the separation efficiency and heat transfer efficiency of the cyclone. Furthermore, from observing Figure 7b, it can be seen that at the inner cylinder inlet, due to the sudden decrease in cross-sectional area, a large amount of airflow rushing in will cause a sudden increase in velocity. In

particular, in the edge area, after the 'short circuit' airflow enters, it will also be squeezed by the surrounding airflow, with lower freedom and thus higher velocity.

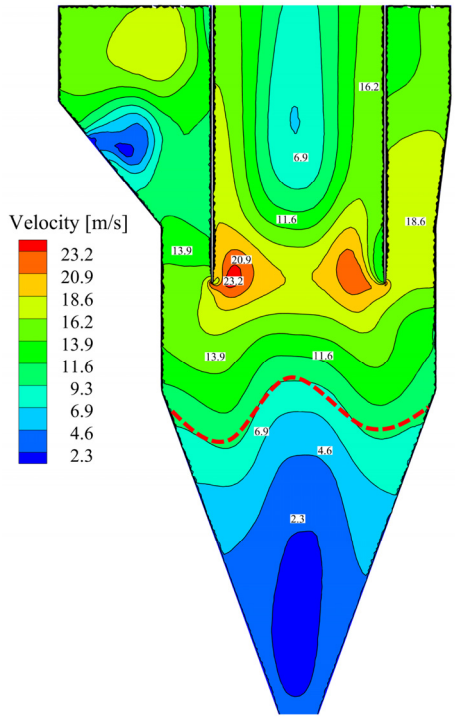


**Figure 6.** Velocity contours of center axial profile.

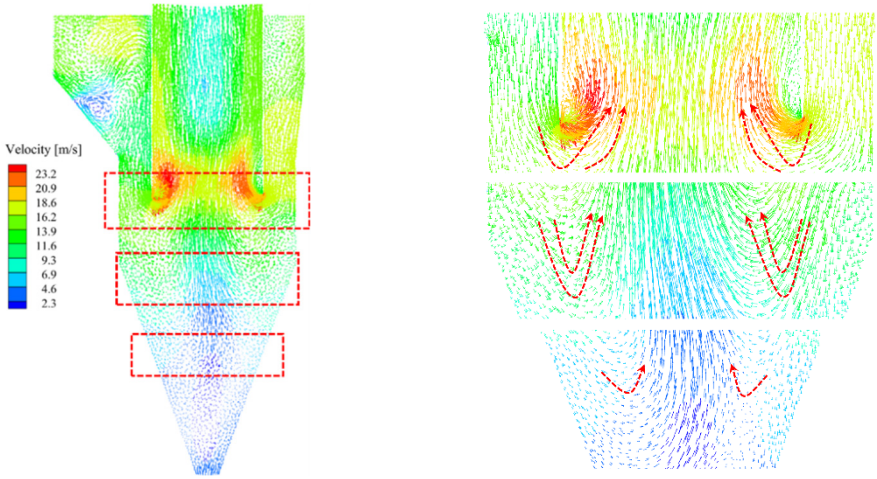


(**a**) (**b**)

**Figure 7.** (**a**) Velocity vectors of center axial profile. (**b**) The partial enlargements.

The air velocity inside a cyclone separator can be decomposed into three component velocities: The tangential velocity formed by the rotary motion, the radial velocity pointing from the outer to the inner towards the center, and the axial velocity going downwards or upwards, influenced by gravity and inlet/outlet pressure difference. Among these, the tangential velocity is the largest component velocity and directly determines the magnitude of the centrifugal force of the barycenter of the air stream, which is the force that particles receive from the inner pointing towards the wall. Its magnitude also directly affects the separation effect of the airflow and particles. The axial velocity affects particle settling and also determines whether the metakaolin will be lifted by the airflow and carried into the exhaust port. The radial velocity is the smallest component velocity, generated by the

centripetal force, which is also the driving force that causes the airflow to change its rotary motion from outer to inner [26].

Figure 8 shows a contour of the tangential velocity of the CC1 cyclone. The three dashed lines in Figure 8 indicate the radial profiles $S_1$, $S_2$, and $S_3$, and the vectors of the tangential velocity at these three sections are drawn, as shown in Figure 9. It can be seen from Figure 8 that due to the asymmetrical inlet of the cyclone volute, the tangential velocity of the airflow is less asymmetrical when it first enters the cyclone, and the tangential velocity of the airflow after the acceleration of the volute reduction is significantly greater than the tangential velocity of the airflow just entering the volute. As the airflow rotates to the cyclone column part, its tangential velocity has shown good symmetry, which indicates that the strong swirl flow of the airflow can gradually reduce the impact of the asymmetrical shell inlet as the airflow moves downward.

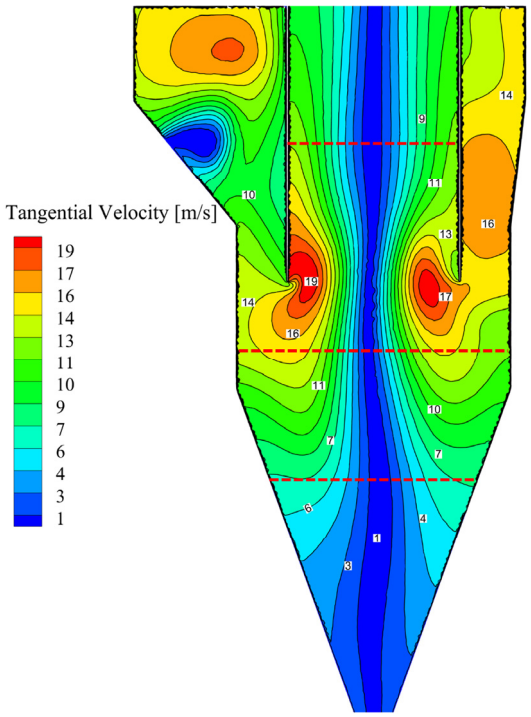


**Figure 8.** Tangential velocity contour.

The combined analysis of Figures 8 and 9 reveals that the rotation direction of the inner and outer swirl is the same, but the tangential velocity of the outer swirl is significantly higher than that of the inner swirl. The maximum tangential velocity in the swirl chamber reaches 20 m/s, which is primarily located near the inner cylinder entrance. Moving downwards, as the outer swirl descends from the cylindrical part to the conical part, the tangential velocity decreases as energy is lost. The airflow that reaches the bottom experiences reflection due to the centripetal force and pressure difference at the entrance and exit of the cyclone and then rises spirally from the bottom center. At this point, the velocity has already decreased to a low value, as seen in Figure 7 where the tangential velocity is lowest near the central axis. By observing each transverse section (section $S_1$, $S_2$, or $S_3$) in Figure 9 from the circumference to the center, it can be seen that the tangential velocity change at the boundary between the inner and outer swirl is significant, showing clear layering.

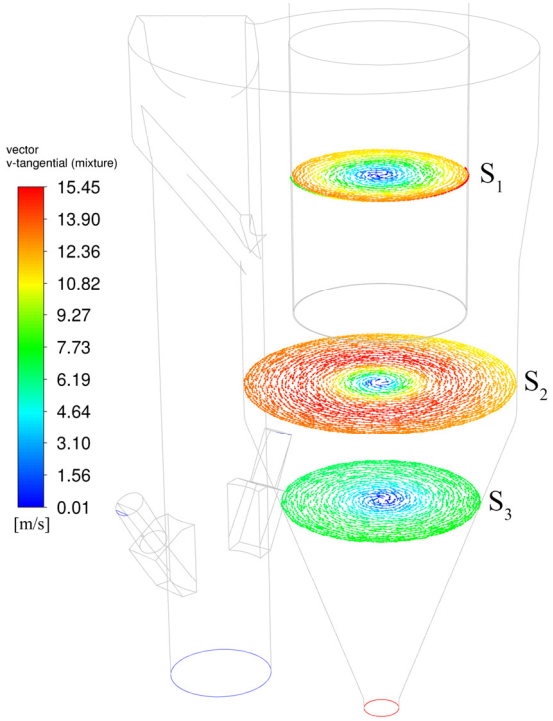


**Figure 9.** Tangential velocity vectors of sections.

Figure 10 shows the axial velocity contour of the CC1 cyclone. Positive values indicate upward velocity and negative values indicate downward velocity. As seen in Figure 10, the overall axial velocity in the cyclone is symmetrically distributed along the center line. The axial velocity of the external swirl flow on the outside is downward, with negative values. The axial velocity of the short-circuit flow and internal swirl flow on the inside is upward, with positive values. Due to the short-circuit flow and the reduction of the inner diameter of the cylinder, the axial velocity near the bottom entrance and in the inner cylinder is obviously higher than in other places, especially since the velocity at the bottom of the inner cylinder is the highest, which is 18.34 m/s. At the bottom of the cyclone, the axial velocity of the airflow is very small, and it will not cause particle second reflux, which can ensure the separation efficiency of the metakaolin.

Figure 11 shows an enlargement of section $S_2$ in Figure 9. Figure 12 shows the axial velocity contour of section $S_2$. A central line is taken from section $S_2$ shown in Figure 9, and the distributions of tangential and axial velocity along the line are shown in Figure 13. As can be seen from Figure 13, a typical Rankine vortex combination vortex distribution is found in the tangential velocity distribution [27]. The tangential velocity shows a peak at the edge of the inner vortex and the outer vortex, that is, the tangential velocity of the airflow increases first and then decreases with the increase in the distance of the flow from the rotational center. This trend distribution causes the particles near the inner vortex to gradually tend to be thrown to the outer vortex and also makes the particles near the wall surface gradually free from the constraint of the flow, which is obviously beneficial for particle and flow separation. Combining Figures 7b, 8 and 10, it can be understood that the peak value on the distribution of tangential velocity is caused by the 'short circuit flow'. The view from the peak towards the wall shows the velocity will slightly decrease due to the resistance near the wall. Looking from the peak value towards the center, when the outer vortex transforms into the inner vortex, the speed will experience a sudden change.

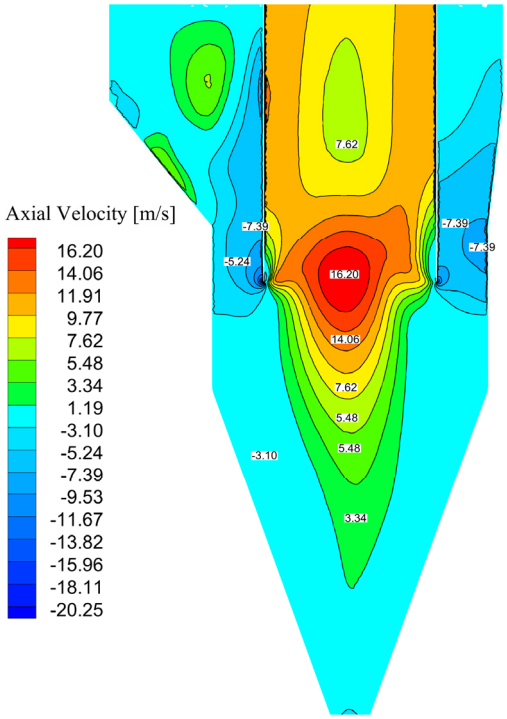


**Figure 10.** Axial velocity contour of center axial profile.

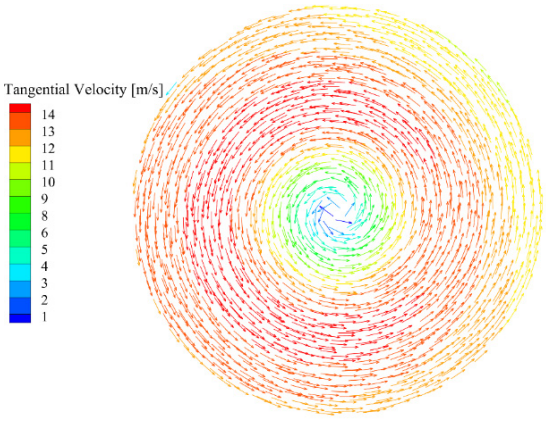


**Figure 11.** Tangential velocity vector of $S_2$ section.

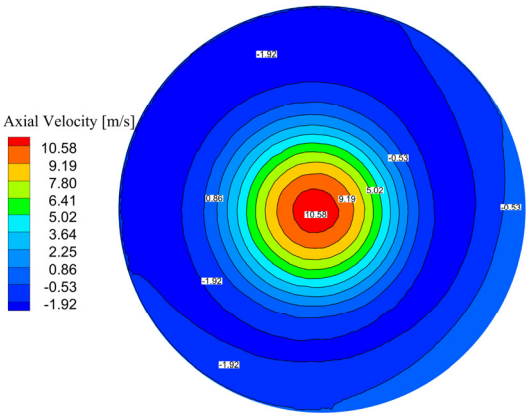


**Figure 12.** Axial velocity contour of $S_2$ section.

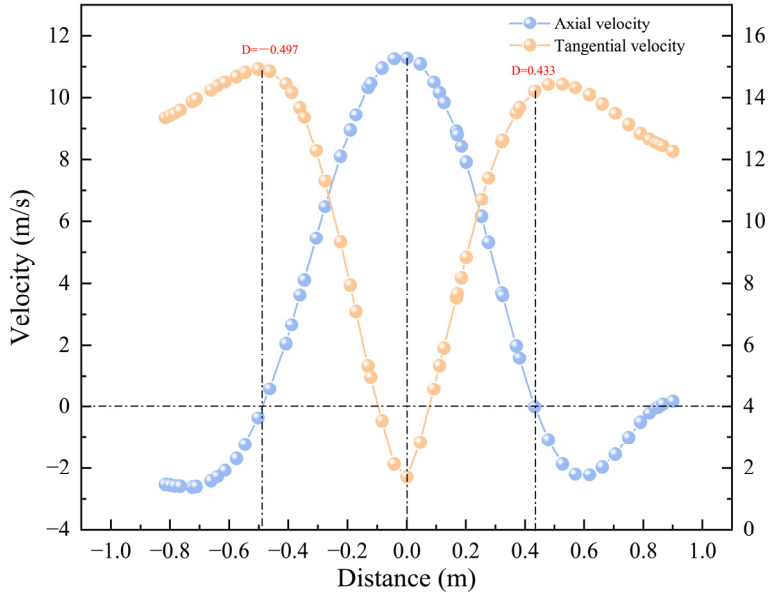


**Figure 13.** The distributions of tangential and axial velocity along the line in the $S_2$ section.

The axial velocity of airflow is positive in the interval −0.497~0.433 m, which indicates the direction of velocity is upward and airflow in this area is the inner vortex. The axial velocity of the airflow in the rest of the area is directed downwards and is the outer vortex. Comparing the two curves in Figure 13, it can be seen that the tangential velocity of the airflow starts to decrease at the exact point where the axial velocity changes from a negative to a positive value, demonstrating the transformation process between inner and outer swirling flows.

Figures 14 and 15 are the contours of the radial velocity of the CC1 cyclone axial profile and transversal profile, respectively, and Figure 16 shows the velocity vector of section $S_4$ in Figure 15. As seen in Figure 14, the radial velocity is highest near the wall of the bottom of the inner cylinder, which is due to the phenomenon of 'short circuit flow'. The magnitude of the radial velocity in the rest of the region is small. As can be seen in Figure 15, the average radial velocity gradually decreases in each cross-section from top to bottom. In each cross-section, there are areas of very low radial velocity in the vicinity of the center, which is caused by the rotation of the inner swirling flow. In combination with Figures 15 and 16, it can be seen that in $S_4$, the vast majority of the radial velocity of the airflow is directed toward the center of this cross-sectional circle, as a result of the wall constraint. However, there is a small area near the center where the radial velocity points towards the wall, which is a result of the inward swirling flow.

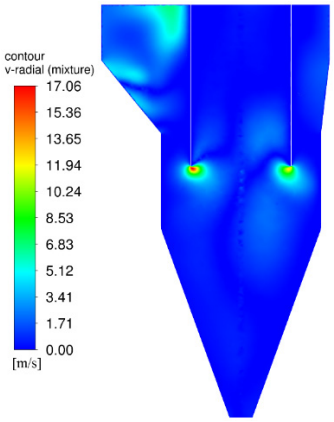


**Figure 14.** Radial velocity contour of center axial profile.

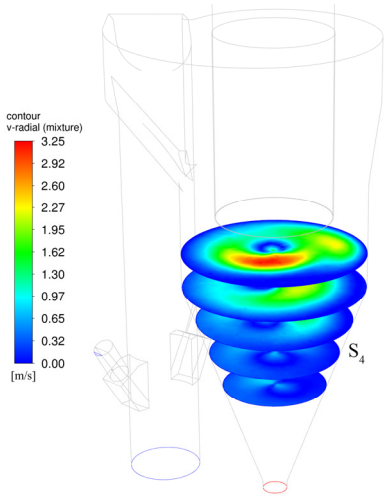


**Figure 15.** Radial velocity contour of cross-sections.

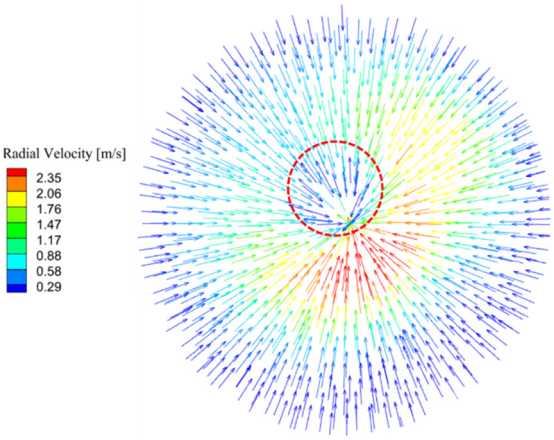


**Figure 16.** Radial velocity vector of $S_4$.

Figure 17 shows the streakline of the airflow in the CC2 heat exchanger, and the color represents the velocity magnitude. Figure 18 is the velocity contour of the end section of the heat exchanger. By combining Figures 17 and 18, it can be seen that the airflow rotates out of the CC1 outlet into the heat exchanger duct of CC2 and continues to rotate upwards, then passes through the at different speeds into the two cyclones. The contour shows that the velocity of airflow on the right side of the heat exchanger is obviously higher than that on the left side, which also indicates that the airflow volume in the right cyclone will be higher than that in the left cyclone. In fact, the statistics show that the airflow mass flow entering the left and right cyclones are 8.5 kg/s and 10.7 kg/s, respectively, that is, deviated flow occurs. Figure 19 shows the particle-phase volume fraction contour at the volute inlets, and the numbers are the particle-phase mass flow passing through the section per second. By combining Figures 18 and 19, it can be found that the particle-phase mass flow in the left and right cyclones is different. More heat particles and less cold air enter the left cyclone, while the situation is exactly the opposite in the right cyclone. This will inevitably affect the gas–solid heat transfer in CC2 cyclones and may cause more serious temperature deviation.

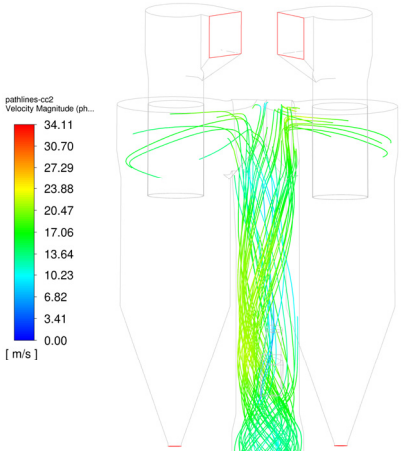


**Figure 17.** Gas streaklines in CC2 heat exchanger.

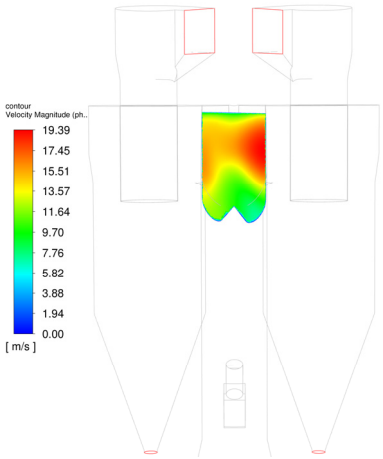


**Figure 18.** Velocity contour of end section of CC2 heat exchanger.

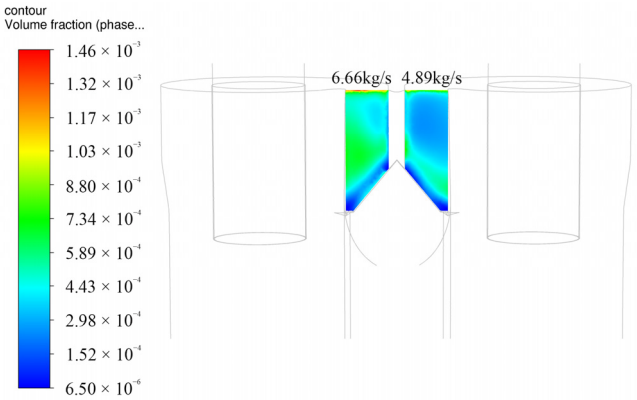


**Figure 19.** Particle-phase volume fraction contour at the volute inlet.

Due to the similarity of fluid motion patterns in cyclone separators, the flow field in the CC2 cyclone separator will not be discussed further.

### *5.2. Temperature Field*

In this section, the temperature field of the cyclones will be analyzed briefly. Taking the CC1 cyclone as an example, the temperature contour of the CC1 cyclone is shown in Figure 20. Upon comparing Figures 6, 7 and 20, it is evident that the temperature distribution inside the cyclone exhibits a certain degree of symmetry, except at the cyclone inlet. The gas–solid heat exchange continues to occur inside the cyclone, as observed by the

distinct temperature differences among the outer cyclone streams at varying heights. As illustrated in Figure 7, as the airflow rotates downwards, the outer airflow is continuously transformed into an inner airflow by the pressure difference between the inside and outside, which then exits through the exhaust port. This results in temperature stratification inside the cyclone from top to bottom and from outside to inside. The shape of the boundary layer is nearly identical to the trajectory of the airflow vector diagram depicted in Figure 7b.

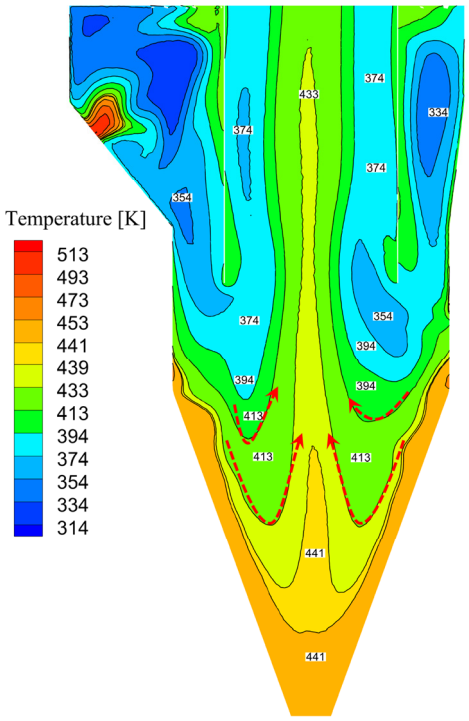


**Figure 20.** The temperature contour of CC1 cyclone.

In terms of temperature variation, the temperature of the airflow that transforms into the inner spiral flow later is higher, which is due to its longer contact time with the hot metakaolin. Part of the airflow, called the short-circuit flow, leaves the CC1 cyclone before sufficient hot metakaolin exchange has taken place. This not only takes away some of the metakaolin particles and reduces the separation efficiency of the CC1 cyclone but it also takes away the cooling airflow and reduces the cooling effect of the cyclone. Reducing the occurrence of short-circuit flow is a key measure to improve the separation efficiency of this cyclone, as well as the cooling effect.

As shown in Figure 21, a similar stratification of the temperature distribution at the CC1 gas outlet is clear, as shown in Figure 6. The temperature distribution in this section exhibits a pattern of higher temperatures in the center and lower temperatures towards the outer regions. In combination with Figure 20, this temperature distribution is well explained: The high-temperature zone in the middle is the result of the part of the inner swirling flow that moves to the bottom of the cyclone before folding back, and this part of the flow is in contact with the metakaolin particles for the longest time and receives the most heat. The lowest temperature zone near the outside is caused by 'short circuit flow'. At the same time, most of the hot metakaolin carried by these 'short circuit flow' will rotate around the inner cylinder wall due to centrifugal forces, as shown in Figure 21b. These particles can still provide heat to the airflow, resulting in an increase in temperature in the outermost region.

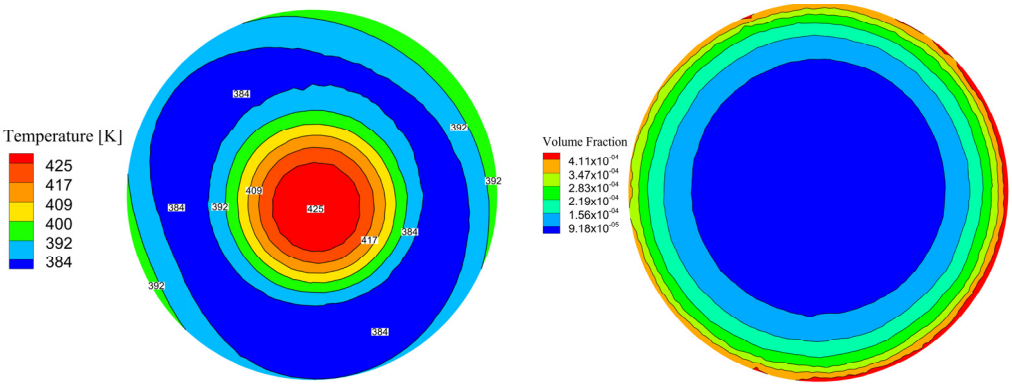


(**a**) (**b**)

**Figure 21.** The contours of CC1 gas outlet. (**a**) Temperature contour. (**b**) Volume fraction contour of particle phase.

Figure 22 depicts three different gas streaklines: (a) represents a 'short circuit flow', (b) represents a flow that transitions from outer to inner swirling flow during downward movement, and (c) represents a flow that recirculates when it reaches the bottom of the cyclone. These three types correspond to the three motion states depicted in Figure 7b, indicating that the temperature of the airflow entering the inner cylinder of this cyclone is determined by its motion state. As shown in this figure, the short-circuit flow entering the inner cylinder of the cyclone has a relatively low temperature, which inevitably leads to a decrease in the cooling effect of the cyclone. To enhance the cooling effect of the cyclone under the same boundary conditions, a structural modification of the cyclone can be considered to reduce the occurrence of short-circuit flow.

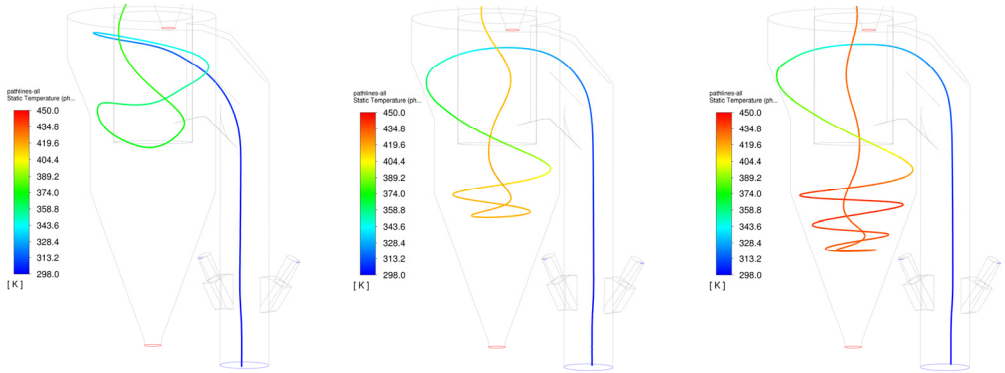


(**a**) (**b**) (**c**)

**Figure 22.** The streaklines of three different types of airflow. (**a**) Airflow with short-circuit flow occurring directly. (**b**) Airflow with short-circuit flow occurring during downward motion. (**c**) Airflow without short-circuit flow occurring.

Figure 23 presents the streakline and the contour of the CC2 heat exchanger tube, demonstrating its heat transfer process. As shown in Figure 23b, due to the high air volume and short residence time in the heat exchanger tube, the cold air near the tube wall does not come into full contact with the hot metakaolin until there are still large areas of low temperature at the exit of the heat exchanger tube. Furthermore, the temperature difference between the airflow into the two cyclones is apparent due to the influence of airflow rotation, resulting in the occurrence of a biased temperature phenomenon.

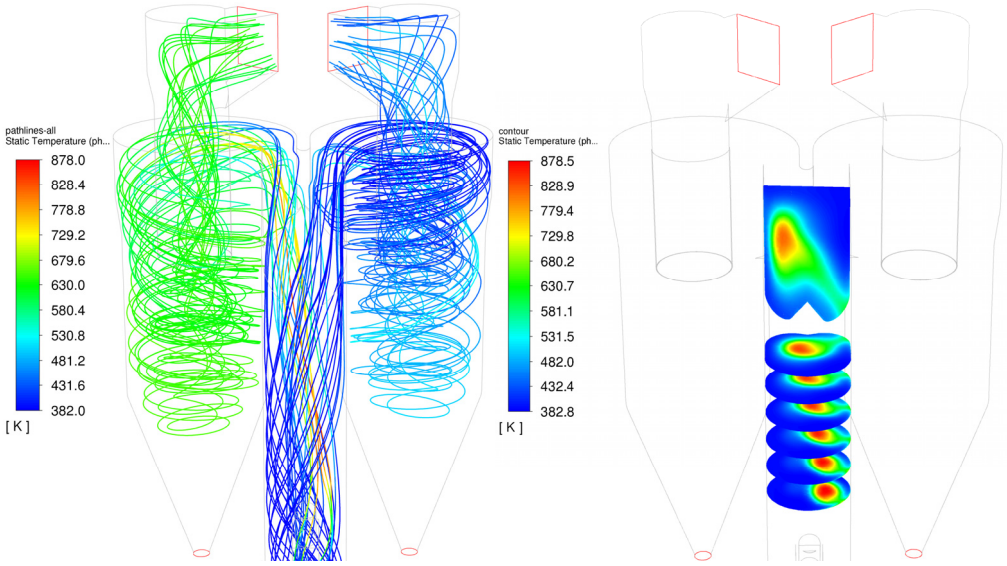


**Figure 23.** Heat transfer in the CC2 heat exchanger. (**a**) Streakline of gas. (**b**) Temperature contour.

Finally, the average temperature of each outlet obtained from the above simulation is shown in Table 6. As can be seen from Table 6, the cooling system can cool the kaolin calcination product at 910 K to 442 K by a gas–solid heat exchange; however, the excessive cooling air volume results in a high gas–solid temperature difference of approximately 50 K at the exit of the individual cyclones. The inadequate heat exchange between the gas and solid in the CC2 heat exchanger tube, the excessive rotation of the airflow, and the short contact time between the gas and solid phases all result in the appearance of the bias flow and temperature in the CC2 cyclone. The installation of a rectifier at the airflow inlet of the CC2 heat exchanger [28], an additional cyclone for the cooling system, etc., may eliminate this undesirable phenomenon.

**Table 6.** The temperature of the outlet.

| Boundary Type | CC1 | | CC2 | | | |
|---|---|---|---|---|---|---|
| | Gas-Outlet | Particle-Outlet | Gas-Outlet (L) | Particle-Outlet (L) | Gas-Outlet (R) | Particle-Outlet (R) |
| Temperature (K) | 390 | 442 | 617 | 661 | 471 | 532 |

## 6. Conclusions

This paper focuses on the cyclone cooling system in the kaolin suspension calcination production line designed by CBMI Construction Co., Ltd. using CFD technology to analyze the airflow flow patterns.

(1) The airflow enters the CC1 cyclone from the bottom of the heat exchanger in a vertical direction and forms the outer swirling flow between the inner and outer shells of the volute, and after rebounding at the bottom, forms the inner swirling flow that leaks out of the inner shell. The leaked airflow continues to spiral up in the CC2 heat exchanger and enters two cyclones in CC2. Finally, it leaks out from the CC2 outlet. The simulated fluid motion conforms to the actual rules, indicating the rationality of the simulation results.

(2) In the CC1 cyclone, when the airflow spiral descends to the height of the bottom of the inner tube, the airflow begins to diverge. That is, the part of the airflow that moves closer to the wall of the inner cylinder enters the inner cylinder directly, forming a short-circuit flow. The remaining airflow gradually moves downward and transforms from an outer swirling flow to an upward inner swirling flow, and then exits through the gas outlet. The later the occurrence of this transition, the higher the temperature of the airflow entering

the inner cylinder. This is also the reason why the temperature at the exhaust port of the CC1 cyclone shows a distribution of low surroundings and a high center.

(3) There is evident temperature deviation and flow deviation in the twin-cylinder cyclone (CC2), which is primarily due to the high cooling air volume and high rotation of air flow coming from the gas outlet of the CC1 cyclone. A rectifier can be installed at the inlet of the CC2 cyclone to suppress this phenomenon.

**Author Contributions:** Conceptualization, J.X. and Y.D.; Methodology, S.X., S.M., F.H., Y.D., C.Z. and X.Z.; Software, S.X.; Validation, S.M., F.H. and C.Z.; Formal analysis, S.X.; Investigation, R.L., X.Z.; Data curation, S.X.; Writing—original draft, S.X.; Visualization, S.X.; Writing—review & editing, S.M.; Supervision, J.X.; Project administration, R.L., C.Z. All authors have read and agreed to the published version of the manuscript.

**Funding:** This research was funded by CBMI Construction Co., Ltd. under grant number CBMI-EN-220302-2.

**Data Availability Statement:** Data are contained within the article.

**Conflicts of Interest:** The authors declare no conflict of interest.

## References

1. Karatas, M.; Benli, A.; Arslan, F. The effects of kaolin and calcined kaolin on the durability and mechanical properties of self-compacting mortars subjected to high temperatures. *Constr. Build. Mater.* **2020**, *265*, 120300. [CrossRef]
2. WBCSD; IEA. *Technology Roadmap 2009: Carbon Emissions Reductions up to 2050*; IEA: Paris, France, 2009.
3. Harris, D. *Chinese Fly Ash: Supply and International Trading*; World Coal Ash: Sandy, UT, USA, 2015; p. 921.
4. Rasmussen, K.E.; Moesgaard, M.; Køhler, L.L.; Tran, T.T.; Tran, J. Comparison of the pozzolanic reactivity for flash and soak calcined clays in Portland cement blends, Calcined Clays for Sustainable Concrete. In Proceedings of the 1st International Conference on Calcined Clays for Sustainable Concrete, Lausanne, Switzerland, 23–25 June 2015; Springer: Dordrecht, The Netherlands, 2015; pp. 151–157.
5. Tang, S.; Wu, J.; Song, H.; Wang, B.; Sui, T. Research and Design of Suspension Calcining Technology and Equipment for Kaolin, Calcined Clays for Sustainable Concrete. In Proceedings of the 3rd International Conference on Calcined Clays for Sustainable Concrete, New Delhi, India, 15–17 October 2019; Springer: Singapore, 2020; pp. 179–189.
6. Junli, L. Optimisation of New Dry Process Cement Production Technology and Application of Energy Saving Technology. *Sichuan Cem.* **2020**, *3*, 1.
7. An, W.; Chen, T.X. Study on a New Suspension Calcination Technique of Kaolin. *Min. Process. Equip.* **2008**, *36*, 94–96.
8. Rhodes, M. *Introduction to Particle Technology*; John Wiley and Sons: West Sussex, UK, 2008.
9. Graham, L.J.; Taillon, R.; Mullin, J.; Wigle, T. Pharmaceutical process/equipment design methodology case study: Cyclone design to optimize spray-dried-particle collection efficiency. *Comput. Chem. Eng.* **2010**, *34*, 1041–1048. [CrossRef]
10. Zhao, B.; Su, Y.; Zhang, J. Simulation of gas flow pattern and separation efficiency in cyclone with conventional single and spiral double inlet configuration. *Chem. Eng. Res. Des.* **2006**, *84*, 1158–1165. [CrossRef]
11. Fatahian, H.; Fatahian, E.; Nimvari, M.E.; Ahmadi, G. Novel designs for square cyclone using rounded corner and double-inverted cones shapes. *Powder Technol.* **2021**, *380*, 67–79. [CrossRef]
12. Zhao, Q.; Cui, B.; Wei, D.; Song, T.; Feng, Y. Numerical analysis of the flow field and separation performance in hydrocyclones with different vortex finder wall thickness. *Powder Technol.* **2019**, *345*, 478–491. [CrossRef]
13. Yong, S. *Numerical Simulation of Gas-Solid Two Phase Flow in Cyclone Separator*; Northeastern University: Shenyang, China, 2011.
14. Nakhaei, M.; Lu, B.; Tian, Y.; Wang, W.; Dam-Johansen, K.; Wu, H. CFD Modeling of Gas–Solid Cyclone Separators at Ambient and Elevated Temperatures. *Processes* **2020**, *8*, 228. [CrossRef]
15. Salakhova, E.I.; Zinurov, V.E.; Dmitriev, A.V.; Salakhov, I.I. Modeling of Erosion in a Cyclone and a Novel Separator with Arc-Shaped Elements. *Processes* **2023**, *11*, 156. [CrossRef]
16. Pang, X.; Wang, C.; Yang, W.; Fan, H.; Zhong, S.; Zheng, W.; Zou, H.; Chen, S. Numerical simulation of a cyclone separator to recycle the active components of waste lithium batteries. *Eng. Appl. Comput. Fluid Mech.* **2022**, *16*, 937–951. [CrossRef]
17. Ledang, K.; Yoonjoon, Y. A hybrid CFD—Deep learning methodology for improving the accuracy of pressure drop prediction in cyclone separators. *Chem. Eng. Res. Des.* **2023**, *190*, 296–311.
18. Mothilal, T.; Pitchandi, K. Influence of inlet velocity of air and solid particle feed rate on holdup mass and heat transfer characteristics in cyclone heat exchanger. *J. Mech. Sci. Technol.* **2015**, *29*, 4509–4518. [CrossRef]
19. Chlebnikovas, A.; Kilikevičius, A.; Selech, J.; Matijošius, J.; Kilikevičienė, K.; Vainorius, D.; Passerini, G.; Marcinkiewicz, J. The Numerical Modeling of Gas Movement in a Single Inlet New Generation Multi-Channel Cyclone Separator. *Energies* **2021**, *14*, 8092. [CrossRef]
20. Haijian, D. *Numerical Simulation Algorithm of the Thermal Flow Field in a Kiln Inlet Predecomposition System and Its Engineering Application*; Wuhan University of Technology: Wuhan, China, 2009.

21. Jiale, C. *Research and Application of Gas-Solid Two Phase Flow in 6000T/D Cyclone Preheater*; Wuhan University of Technology: Wuhan, China, 2017.
22. Almohammadi, K.M.; Ingham, D.B.; Ma, L.; Pourkashan, M. Computational fluid dynamics (CFD) mesh independency techniques for a straight blade vertical axis wind turbine. *Energy* **2013**, *58*, 483–493. [CrossRef]
23. John, D.A. *Computational Fluid Dynamics*; China Mechine Press: Beijing, China, 2019.
24. Zhang, K.; Tao, C.; Wang, H.; Liu, J. Study on Experiment and Simulation for Preheater Dispersing Box. *Cem. Technol.* **2014**, *1*, 22–24.
25. Fluent Inc. *ANSYS Fluent User's Guide*; Fluent Inc.: New York, NY, USA, 2021.
26. Hongzhou, J. *Thermal Equipment for Inorganic Non-Metallic Materials*; Wuhan University of Technology Press: Wuhan, China, 2015; pp. 33–40.
27. Zhongxia, Z. *Numerical Simulation and Optimization of a Primary Cyclone Preheater for a Gaseous Suspension Roaster*; Central South University: Changsha, China, 2008.
28. Tingxin, C.; Shaowu, J.; Qi, L.; Yanfei, Y. A Cyclone Inner Cylinder Based on a Standard Type Rectifier. China Patent CN204769196U, 29 May 2015.